

Computational Predictions of the Hypersonic Material Environmental Test System Arc-Jet Facility

Andrew J. Brune* Walter E. Bruce, III[†]

David E. Glass[‡] Scott C. Splinter[§]

NASA Langley Research Center, Hampton, VA, 23681

The Hypersonic Materials Environmental Test System arc-jet facility located at the NASA Langley Research Center in Hampton, Virginia, is primarily used for the research, development, and evaluation of high-temperature thermal protection systems for hypersonic vehicles and reentry systems. In order to improve testing capabilities and knowledge of the test article environment, a detailed three-dimensional model of the arc-jet nozzle and free-jet portion of the flow field has been developed. The computational fluid dynamics model takes into account non-uniform inflow state profiles at the nozzle inlet as well as catalytic recombination efficiency effects at the probe surface. Results of the numerical simulations are compared to calibrated Pitot pressure and stagnation-point heat flux for three test conditions at low, medium, and high enthalpy. Comparing the results and test data indicates an effectively fully-catalytic copper surface on the heat flux probe of about 10% recombination efficiency and a 2-3 kPa pressure drop from the total pressure measured at the plenum section, prior to the nozzle. With these assumptions, the predictions are within the uncertainty of the stagnation pressure and heat flux measurements. The predicted velocity conditions at the nozzle exit were also compared and showed good agreement with radial and axial velocimetry data.

*Aerospace Engineer, Structural and Thermal Systems Branch, Mail Stop 431, AIAA Member.

[†]Thermal Lead, Structural and Thermal Systems Branch, Mail Stop 431.

[‡]Project Engineer, Structural Mechanic and Concepts Branch, Mail Stop 190.

[§]Aerospace Engineer, Structural Mechanic and Concepts Branch, Mail Stop 190.

Nomenclature

A	Cross-sectional area of the nozzle inlet (plenum), cm ²
C	Conversion coefficient in the bulk enthalpy energy balance, 6.315x10 ⁻⁵ min-m ³ /s-gal
C_p	Specific heat based on constant pressure, J/kg-K
C_w	Cooling water flow rate, gal/min
c_i	Mass fraction of species i
E	Arc heater voltage, volts
H	Enthalpy, MJ/kg
H_o	Total enthalpy, MJ/kg
I	Arc heater current, amps
l	Length of the copper slug, cm
M_{total}	Total mass flow rate, kg/sec
P	Pressure, kPa
P_{box}	Test cabin pressure, Pa
\dot{q}	Heat flux, W/cm ²
r	Radius from plenum centerline, cm
R_B	Base radius of the calibration probe, cm
R_N^{eff}	Effective nose radius of the calibration probe, cm
T	Temperature, K
t	Time, sec
u	Axial velocity, m/sec
X	Axial distance from the nozzle inlet (plenum), cm
Z	Radial distance from the nozzle centerline, cm
Δ	Differential operator
ρ	Density, kg/m ³

Subscripts

CL	Centerline of the plenum
CW	Cooling water
Cu	Copper
$FCCW$	Fully-catalytic cold wall
ref	Reference condition
w	Wall condition

I. Introduction

Thermal protection systems (TPS) are being developed and tested at NASA Langley Research Center in the Hypersonic Materials Environmental Test System (HyMETS) arc-jet facility for application on hypersonic vehicles and reentry systems. Ground testing of relevant materials is essential to develop, screen, and demonstrate their performance at flight-relevant conditions. Development of codes to model the TPS thermal response for various flight conditions, other than those within limited operating envelopes of ground facilities, is also supported by testing efforts.

The HyMETS facility was installed at NASA Langley Research Center in 1968 as a 100 kW segmented-constrictor-direct-current-electric-arc-heated wind tunnel. The facility was used primarily for emissivity, catalysis, and dynamic oxidation testing of metals and coatings for hypersonic vehicles from the 1970s through the early 2000s [1–3]. Upgrades were made to the facility test conditions, which included increased capability to test specimens at higher surface temperatures and pressures [4]. Since then, HyMETS has been used primarily for characterization of ceramic matrix composite materials, rigid and flexible TPS, high-temperature coatings, and for performing research and development on plasma flow diagnostics.

Of the limited number of facilities available to currently support TPS development and evaluation, arc-jet facilities can provide the most relevant aerothermal loads on material systems for durations sufficient to test over the total flight heat load. Challenges arise from these facilities, which include determination and verification of appropriate arc-jet conditions and test model configurations at sufficiently approximate flight loads. Computational fluid dynamics (CFD) analysis frameworks have been developed for NASA Ames arc-jet facilities, including the Aerodynamic Heating Facility (AHF) and the Interaction Heating Facility (IHF), using radial sweep information to construct the inflow states [5]. Other arc-jet facilities, which include HyMETS, have limited information from the stagnation probe measurements along the stagnation streamline and require reconstructive assumptions about the inflow state based on limited calibration data. A paper by Mazaheri [6] introduced a methodology to estimate the flight-relevant heat flux and heat load and predict the relationship between the flight and arc-jet surface heat flux. The method uses a simplified approach to determine the arc-jet flow conditions consistent with the lumped pressure and bulk enthalpy, assuming equilibrium theory through the nozzle and eliminating the need to simulate this portion of the arc jet. A representative freestream condition is estimated that satisfies the cold-wall heat flux and surface pressure measured by the calibration probe.

This paper presents an alternative method to the simplified method described above [6]. The alternative method involves the direct simulation of the arc-jet facility, including the arc-jet nozzle and test cabin. The

difference between the two methods is the process to obtain the relevant arc-jet conditions, just upstream of the calibration probe, using some form of CFD modeling. The technique presented in this work requires knowledge of the measured total pressure and bulk enthalpy consistent with the arc-jet heater current and flow rate setting. As will be shown in this paper, there is a degree of non-uniformity of the flow throughout the arc-jet nozzle and test cabin. The non-uniform arc-jet flow profiles at the plenum, prior to the nozzle, are predicted to satisfy the surface heat flux and pressure measured by the calibration probe. The advantage of this approach is the direct simulation of the actual thermal nonequilibrium flow and its non-uniformity through the nozzle and test cabin to determine the appropriate arc-jet conditions upstream of the TPS sample. Once the CFD predictions that closely represent the measured calibration data are obtained, flight-to-ground comparison and evaluation of specimens can be made using the flow-field profiles prior to the TPS sample. This final step is left for a future study.

This paper is organized to first present an overview of the HyMETS facility configuration and instrumentation. The next section presents the methodology that determines the actual plenum flow profiles consistent with the measured arc-jet heat flux and pressure. The following section validates the methodology by comparing computed and measured arc-jet data for a particular test condition. The last section applies the methodology to a range of arc-jet conditions at low, medium, and high enthalpy.

II. HyMETS Arc-jet Facility

The HyMETS facility, shown in Fig. 1 in its entirety, uses a segmented-constrictor-dc-electric-arc-heater as an arc heater generator with N_2 and O_2 injected as the test gas. The arc heater generator can be visualized in Fig. 2 and 3 and is mounted on the outside of the test cabin door. The generator consists of water-cooled components, which include a copper cathode with tungsten button emitter, electrically-isolated copper segment constrictors with a 1.27-cm (0.5-in) diameter bore, and a copper divergent-ring anode. Test gasses are injected tangentially into the bore of the arc heater generator at six discrete locations and can be custom mixed to desired atmospheric composition. The gasses are heated by a high-voltage electric arc that is maintained between the cathode and anode to create a high-temperature dissociated flow. The HyMETS facility has a viewport on the test cabin door to obtain video and pyrometer thermal data of the test specimen, in addition to viewports in the test cabin walls. A detailed description and overview of the HyMETS facility and performance envelopes for stagnation testing can be found in the literature [4, 7].

For stagnation testing, a water-cooled 6.35-cm (2.5-in.) exit diameter conical nozzle, made of copper and attached to the arc heater generator system, is used to provide the appropriate combination of heat flux and model pressure. The high-temperature flow from the arc heater generator is accelerated through the nozzle and exhausted into a 60.9-cm (2-ft) wide by 91.4-cm (3-ft) long vacuum test chamber. The flow proceeds

downstream of the test chamber into a collector cone, a 15.24-cm (6-in.) diameter constant cross-section diffuser, and a coiled-copper tubing heat exchanger to decelerate and cool the flow. The test cabin is pumped to the desired conditions with a mechanical pumping system. Test models are positioned on the centerline of the flow just downstream of the nozzle exit. A TPS test specimen, a Pitot probe, and a slug calorimeter are injected into the flow during each run.



Figure 1: HyMETS facility overview

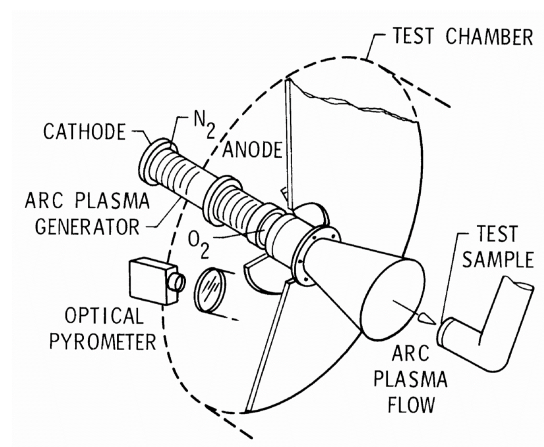


Figure 2: HYMETS test setup schematic

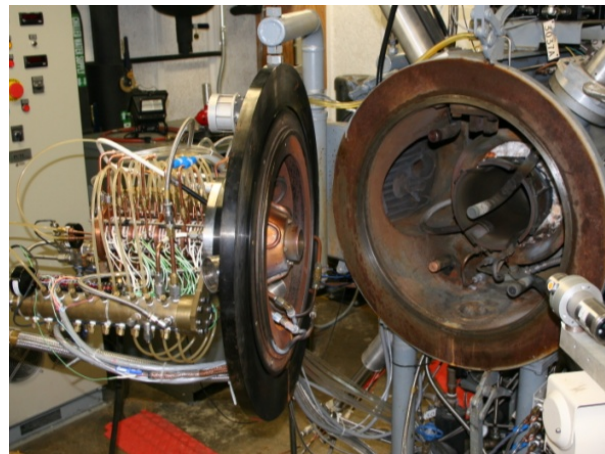


Figure 3: HYMETS facility test setup

A flat-face Pitot probe and copper slug calorimeter [8,9] in Fig. 4 and 5, respectively, are used to determine the flowfield stagnation heat flux and surface pressure during each run. The copper slug calorimeter is used to determine fully-catalytic cold-wall (FCCW) heat flux and consists of an un-cooled slug sensor element that is 1.27-cm diameter by 1.27-cm long (0.5-in. by 0.5-in.) with an uncooled shroud that is 3.3-cm (1.3-in.) diameter by 2.16-cm (0.85-in.) long and a flow-face edge radius of 0.318 centimeters (0.125 inches). The slug sensor element and shroud are fabricated out of oxygen-free high-conductivity (OFHC) copper. The slug sensor element has a 0.005-cm (0.002-in.) wide insulating air gap between it and the shroud, and is held in

place using six cone-tipped set-screws. The slug sensor element also has a Type-K thermocouple mounted on its back surface to measure temperature rise. The length, diameter, and mass of the slug sensor element are measured prior to calorimeter assembly. The copper slug calorimeter is inserted into a steady-state flow for 2-3 seconds so that it achieves a backface temperature rise of several hundred degrees Fahrenheit, not to exceed a final temperature of 588 K (600°F). The FCCW heat flux is calculated from the density of the OFHC copper slug sensor element ρ_{Cu} , the temperature-dependent specific heat capacity of the element $C_p(T)$, the length of the element l , and the slope of the temperature rise $\Delta T/\Delta t$ from the linear portion of the temperature response curve for the Type-K thermocouple using [8]:

$$\dot{q}_{FCCW} = \rho_{Cu} C_{pCu}(T) l \left(\frac{\Delta T_{Cu}}{\Delta t} \right) \quad (1)$$

The uncertainty of the resulting method given by Eq. 1 is assumed to be 10-15% [4,9].

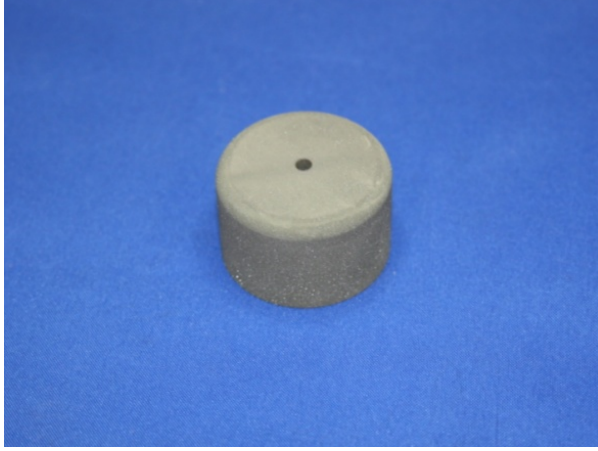


Figure 4: Pitot tube



Figure 5: Copper slug calorimeter

In addition to the surface pressure and heat flux, conditions in the arc jet are measured, including plenum total pressure downstream of the arc heater prior to the nozzle, total mass flow rate, and the average bulk enthalpy at the nozzle exit. An energy balance is performed on the arc heater generator in HyMETS to calculate the bulk enthalpy. The energy input to the arc heater generator is determined by the product of voltage E and current I measurements. The energy removal from the arc heater generator is determined by the product of the cooling water flow rate C_W , and the differential temperature measured across the inlet and outlet of the cooling water manifolds, ΔT_{CW} . Finally, the energy that remains in the arc heater generator is divided by the total measured mass flow rate of the test gases, M_{total} . The bulk enthalpy is calculated using Eq. 2 [10]:

$$H_{bulk} = \frac{EI - CC_W C_{pCW} \rho_{CW} \Delta T_{CW}}{M_{total}} \quad (2)$$

The constant C converts the energy output in the second term to the proper units.

III. Arc-jet Plenum Profile Estimation

In this section, a method to estimate the arc-jet plenum profile conditions consistent with the calibrated cold-wall heat flux and surface pressure is presented. An iterative approach using equilibrium theory at the plenum loosely-coupled with nonequilibrium CFD through the nozzle and test cabin was developed to estimate the arc-jet plenum profile conditions, given the plenum total pressure, bulk enthalpy at the nozzle exit, and calibrated heat flux and surface pressure measured by the slug calorimeter and Pitot probe, respectively. The steps for the iterative process are schematically shown in Fig. 6.

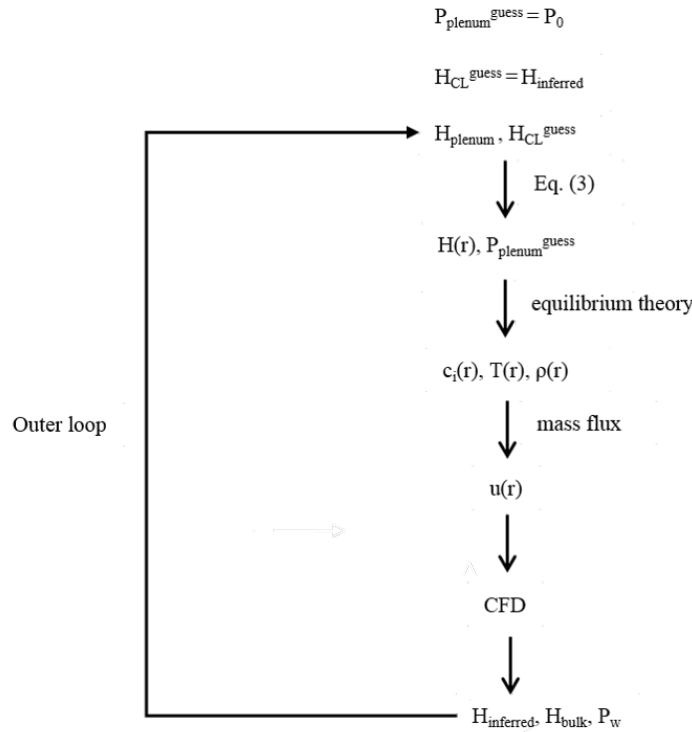


Figure 6: Iterative process for the arc-jet plenum profile condition estimation

In the iterative process, the measured plenum total pressure and the inferred enthalpy computed from the measured surface heat flux and pressure were used to estimate the initial plenum pressure and enthalpy profile. Equilibrium theory was used to estimate the initial plenum profile conditions for the nonequilibrium CFD, which was then used to compute the inferred enthalpy, the enthalpy profile at the nozzle exit, and the surface pressure. The enthalpy profile at the plenum was assumed to have a parabolic shape in mathematical form of Eq. 3:

$$H(r) = a_0 + a_1 r + a_2 r^2 \quad (3)$$

subject to

$$H(0) = H_{CL}^{guess} \quad (4)$$

$$\left. \frac{dH}{dr} \right|_{r=0} = 0 \quad (5)$$

$$\frac{1}{A} \iint_A H(r) = H_{plenum} \quad (6)$$

In Eq. 3, $H(r)$ is the enthalpy profile defined at the plenum and varies with radius r from the nozzle centerline. The coefficients are determined by the conditions from Eq. 4-6, where the centerline enthalpy defines the leading coefficient a_0 , the maximum (peak) enthalpy at the centerline defines coefficient a_1 , and the bulk enthalpy at the plenum defines coefficient a_2 . (Note that the bulk enthalpy at the plenum H_{plenum} is different from the bulk enthalpy at the exit H_{bulk} ; the bulk enthalpy at the plenum is the first term in Eq. 2 without nozzle heat losses.) Given the measured plenum total pressure P_0 and $H(r)$, the remaining thermodynamic state profiles (species mass fractions $c_i(r)$, temperature $T(r)$, and density $\rho(r)$) can be determined assuming thermochemical equilibrium at the plenum. The measured mass flow rate that corresponds to the arc-jet heater pressure and bulk enthalpy can be used to estimate the plenum velocity profile $u(r)$.

The initial plenum profile conditions were then applied to the high-fidelity CFD simulations, which were computed with the LAURA-5 (Langley Aerothermodynamic Upwind Relaxation Algorithm) code [11]. In the CFD simulations, the arc-jet flowfield was modeled with 6-species gas (N_2 , O_2 , NO , N , O , Ar) for low enthalpy flows and 13-species gas (N_2 , O_2 , NO , N , O , Ar , N_2^+ , O_2^+ , N^+ , O^+ , NO^+ , Ar^+ , e^-) for the highest enthalpy condition. Thermal nonequilibrium was modeled by including two energy equations for vibrational and translational modes in the simulations. The calibration probes (Pitot tube and slug calorimeter) are assumed to be at an isothermal cold-wall temperature of 300 K. (Note that the probes are injected for calibration for only a few seconds as discussed in Section II.) The transport and thermodynamic properties in the flow-field environment were computed from species collision integrals [12–14] and curve fit data [15], respectively. Further details on the flow solver and previous applications can be found in the literature [16–22].

Before performing CFD, an axisymmetric computational grid was built with Pointwise using four structured blocks (Fig. 7). The blocks together form a structured mesh that spans the nozzle and surrounding flow around the calibration probes. A grid convergence study was performed and showed that 257 surface normal cells and wall spacing on the order of 10^{-5} was sufficient for reliable heating and pressure predictions

on the calibration probes. As shown in Fig. 7, viscous surfaces were applied on the nozzle and calibration probe surfaces. Non-uniform plenum profiles were used for boundary conditions on the inflow boundary of the nozzle.

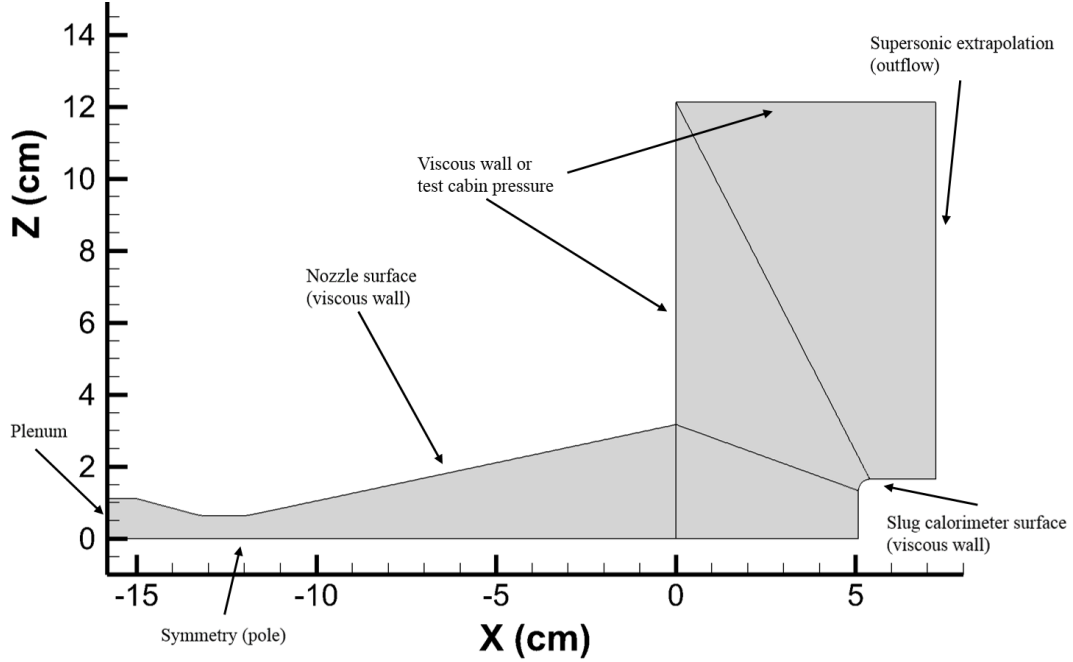


Figure 7: Computational grid layout for arc-jet flow CFD simulations

During the iterative process, the surface pressure P_w , predicted using the initial plenum pressure and the CFD code, was compared with the measured Pitot pressure. Necessary adjustments were made to plenum pressure to match the calibrated pressure value. The inferred enthalpy $H_{inferred}$ and bulk (average) enthalpy H_{bulk} at the nozzle exit, predicted from the CFD code, were then compared to the measured bulk enthalpy and the inferred enthalpy corresponding to the calibrated heat flux and surface pressure. The inferred enthalpy was estimated using an engineering correlation that is a function of the measured probe surface values [23]:

$$H_{inferred} = \frac{2.82\dot{q}_w}{(P_w/R_N^{eff})^{1/2}} + H_w \quad (7)$$

$$R_N^{eff} = 3.33R_B \quad (8)$$

In Eq. 7, R_N^{eff} is an effective hemispherical nose radius corresponding to the calibration probe base diameter R_B . The effective nose radius is estimated using Eq. 8 [24,25]. Furthermore, the wall enthalpy, H_w , is typically considered negligible for an isothermal cold-wall condition. Adjustments in the centerline enthalpy at the plenum were made to match the measured bulk enthalpy and the estimated inferred enthalpy

from Eq. 7.

IV. Arc-jet Flowfield

In the previous section, the methodology to estimate the arc-jet plenum profiles prior to the conical nozzle was presented. An example of the plenum profiles is shown in Fig. 8(a) and 8(b) for an arc-jet bulk enthalpy and plenum total pressure of 6.5 MJ/kg and 109 kPa, respectively. These conditions correspond to the calibrated values tested on the 3.3-cm (1.3-in.) calibration probe for a surface pressure and heat flux of about 5.1 kPa and 107 W/cm², respectively. For this condition, the flow temperature peaks on the centerline at about 5000 K, which corresponds to mostly dissociated O₂. A small amount of N₂ dissociation is observed at this condition. The enthalpy at the plenum centerline was estimated to be 10.5 MJ/kg, which is higher than the estimated inferred enthalpy of 9.7 MJ/kg at the nozzle exit from Eq. 7. This difference can be explained by the heat losses through the water-cooled nozzle. (Note that the bulk enthalpy at the plenum is higher than the bulk enthalpy at the nozzle exit due to the energy balance in Eq. 2.) The plenum pressure was estimated to be 106 kPa to match the probe surface pressure, which is approximately 3.0 kPa drop from the total pressure measured at the plenum. This pressure drop was also seen for other test conditions considered in the next section. Although minor, the drop in pressure is likely due to the gas moving at the plenum, rather than stagnant, and potential uncertainty in the measured total pressure due to blockage with the copper slag from the anode.

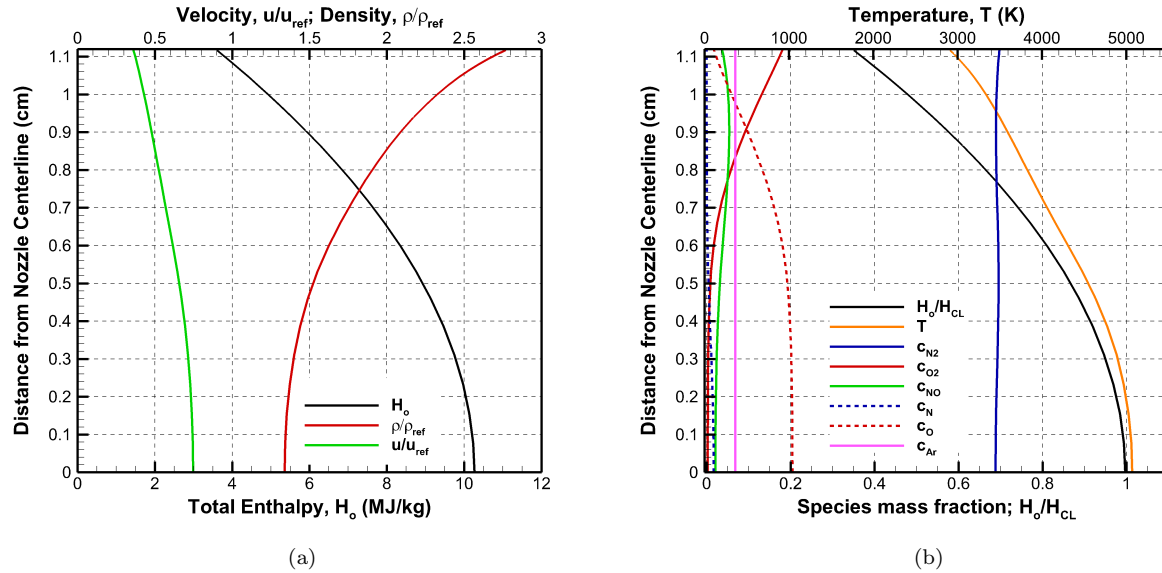


Figure 8: Plenum profiles prescribed to reproduce the 3.3-cm calibration probe heat flux and surface pressure data. 6.35-cm diameter nozzle flow: parabolic enthalpy profile, $H_{CL} = 10.5$ MJ/kg, $P_{plenum} = 106$ kPa

Figure 9 shows an illustration of the computed 6.35-cm nozzle and test cabin flow field. The flow

expands in the nozzle to around Mach 5 at the exit with a computed inferred enthalpy of about 9.5 MJ/kg. Comparing the inferred enthalpy prediction from CFD to the estimated inferred enthalpy from Eq. 7, the plenum centerline enthalpy is verified to correspond with the inferred enthalpy that matches the appropriate combination of calibrated heat flux and surface pressure. In the nozzle, the chemical composition freezes near the throat where the dissociated gas mixture is vibrationally excited. As expected, the computations predict that the flow is chemically and vibrationally frozen before it reaches the nozzle exit, which is shown in Fig. 9(d). Coincidentally, the vibrational and translation temperatures in Fig. 9(c) deviate from equilibrium near the nozzle throat as well. Oxygen remains mostly dissociated within the entire flowfield, except in the boundary layer near the walls, while nitrogen remains in its molecular state. The results inform key differences in the role of total enthalpy in the arc jet compared to flight. In flight, the kinetic energy component of the total enthalpy dominates the internal and chemical enthalpy (enthalpy of formation) components, where the freestream has a low equilibrium temperature with diatomic molecules (N_2 and O_2). In the arc jet, the flow velocity is typically smaller than in flight; however, atomic species in dissociated gas mixture at a vibrationally frozen temperature upon rapid expansion in the nozzle adds to the chemical and internal energy components, respectively, and in some cases, can raise the total enthalpy to flight-like levels.

Continuing at the nozzle exit, computed arc-jet predictions are compared with available arc-jet data from planar laser-induced fluorescence (PLIF) that was performed in HyMETS. Inman et al. [26] performed PLIF of naturally-occurring NO to obtain radial and axial velocity measurements at a test condition similar to the example in this section with a bulk enthalpy of 6.5 MJ/kg and plenum total pressure of 109 kPa. As referenced in the paper, the test cabin pressure was reported to be 228 Pa. Therefore, comparisons were first made with the measured data at this cabin pressure by setting a prescribed pressure on the test cabin boundaries in Fig. 7.

Figure 10 compares the axial velocity flowfield downstream of the nozzle exit with a computed flowfield from LAURA on the top and the interpolated measurement profile from velocimetry data on the bottom. The computed and measured axial velocity profiles both show the flow propagating near the centerline with a constant velocity and expanding a distance away from the centerline. Figure 11 shows distributions of axial velocity at four different stream-wise locations labeled L1-L4. The position of lines L1-L4 are shown as white dashed lines in Fig. 10. Computed axial velocity profiles are compared to the measured velocity profiles at 15 and 228 Pa cabin pressures. The results show that the degree of expansion of the flow, downstream of the nozzle exit, depends on the cabin pressure. At the 228 Pa cabin pressure reported by Inman [26], there is good agreement between the measured and computed velocity profiles. Within 2 cm of the nozzle centerline, the axial velocity is nearly constant and does not appear to be impacted by the change in cabin pressure. The results in Fig. 12 also show no influence of the cabin pressure on the radial velocities within 2-3 cm of

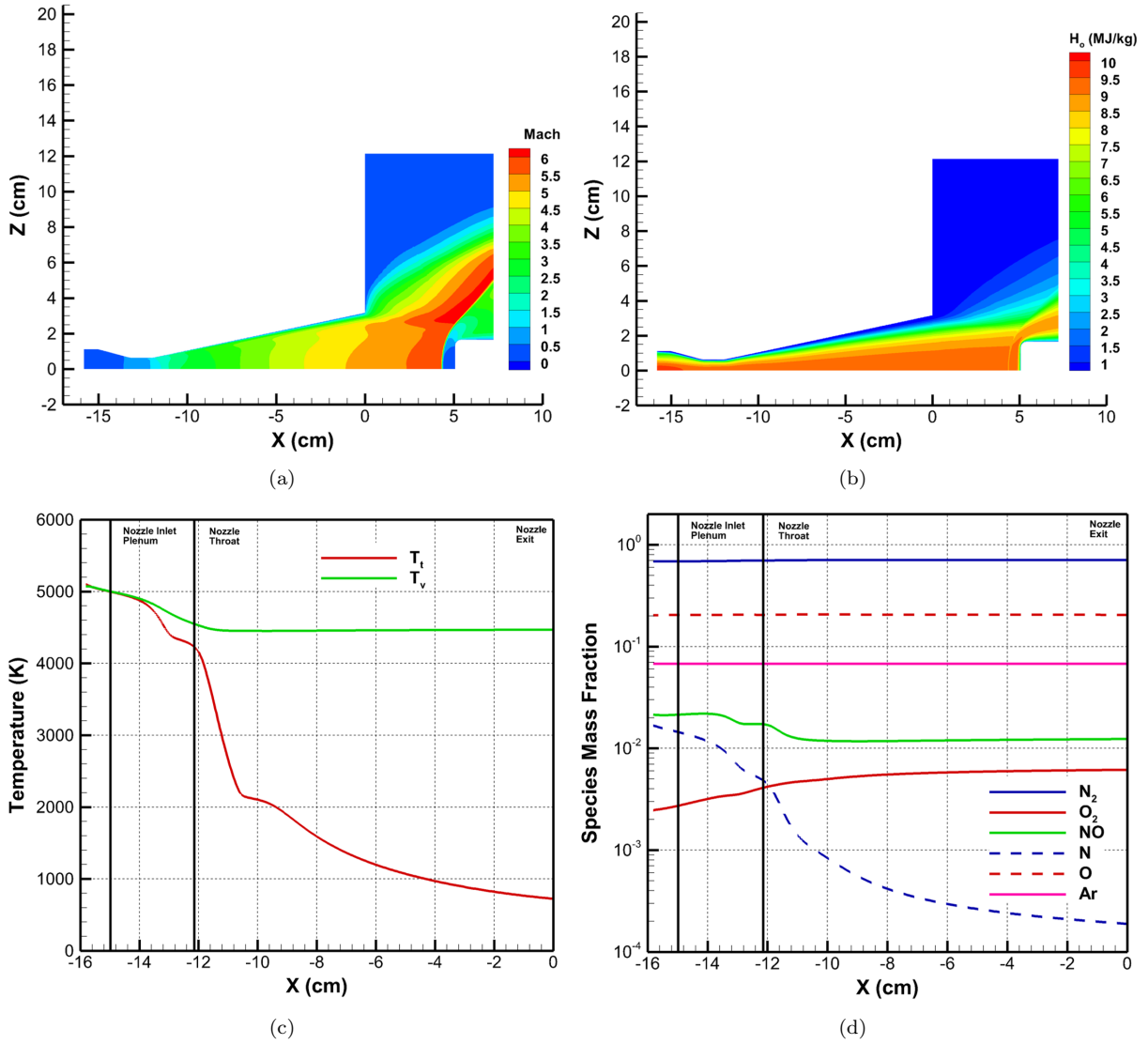


Figure 9: Computed 6.35-cm nozzle flow field including the test cabin and 3.3-cm calibration probes: parabolic enthalpy profile, $H_{CL} = 10.5$ MJ/kg, $P_{plenum} = 106$ kPa

the centerline. Therefore, it is expected that the flow expansion will not impact the surface pressure and heat flux profiles of the calibration probes, because the probes with 1.65 cm radius are well within 2 cm of the centerline. This can be verified by observing the computed surface profiles of the calibration probe in Fig. 13. The x axis shows the radial distance, Z , measured from the center to the edge of the calibration probe. The solid black line represents the calibration probe surface for reference to the surface pressure and heat flux profiles. In this figure, there are minor differences between the surface heat flux and pressure profiles at the 15 and 228 Pa cabin pressure. Therefore, a test model within 2 cm of the nozzle centerline is recommended for minimal unsteady effects from the free-jet expansion in the test cabin. Furthermore, CFD modeling does not require specification of a cabin pressure to obtain a reliable surface solution for calibration probe sizes within this envelope.

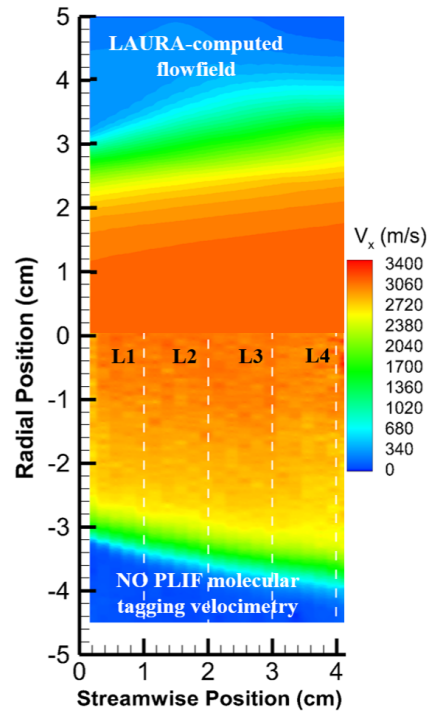


Figure 10: LAURA-computed axial velocity flow field (top) and mean axial velocity field interpolated from molecular-tagging velocimetry profiles (bottom): parabolic enthalpy profile, $H_{CL} = 10.5$ MJ/kg, $P_{plenum} = 106$ kPa, $P_{box} = 228$ Pa

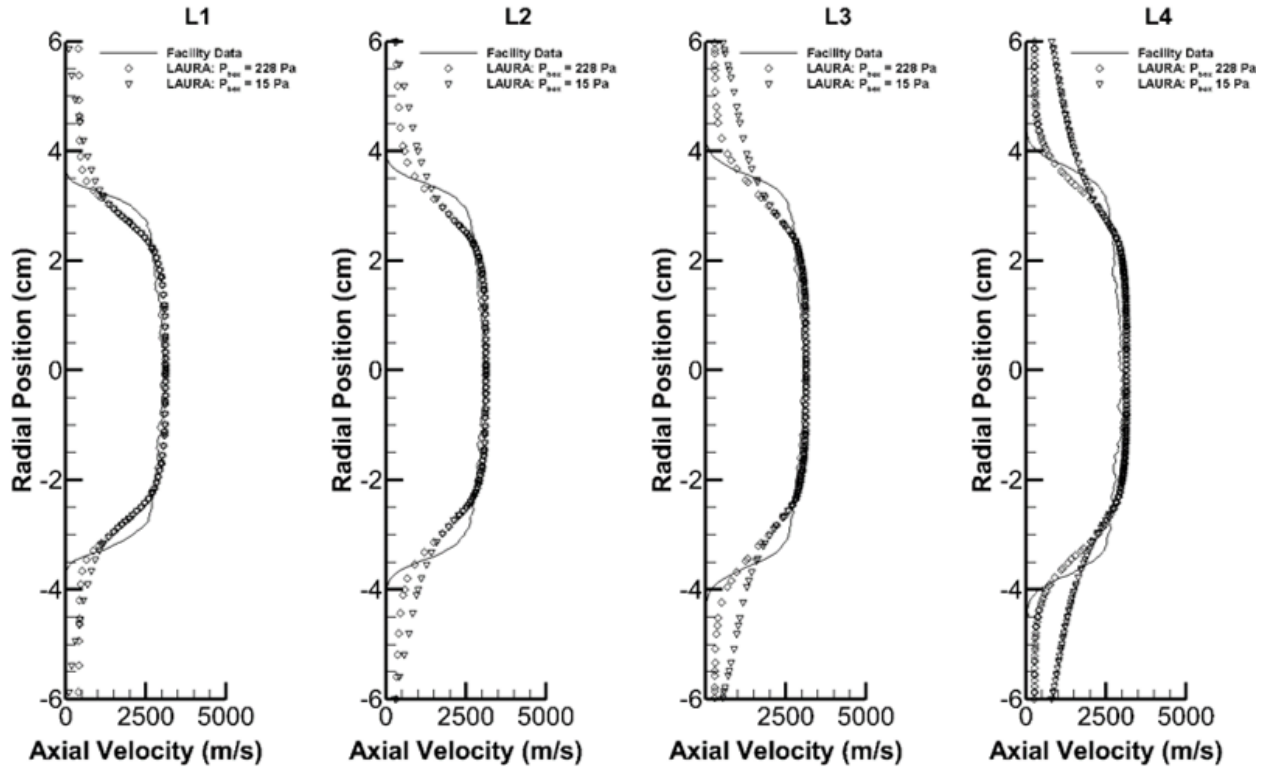


Figure 11: Computed and measured profile distributions of axial velocity: parabolic enthalpy profile, $H_{CL}=10.5$ MJ/kg, $P_{plenum} = 106$ kPa, $P_{box} = 15$ and $P_{box} = 228$ Pa

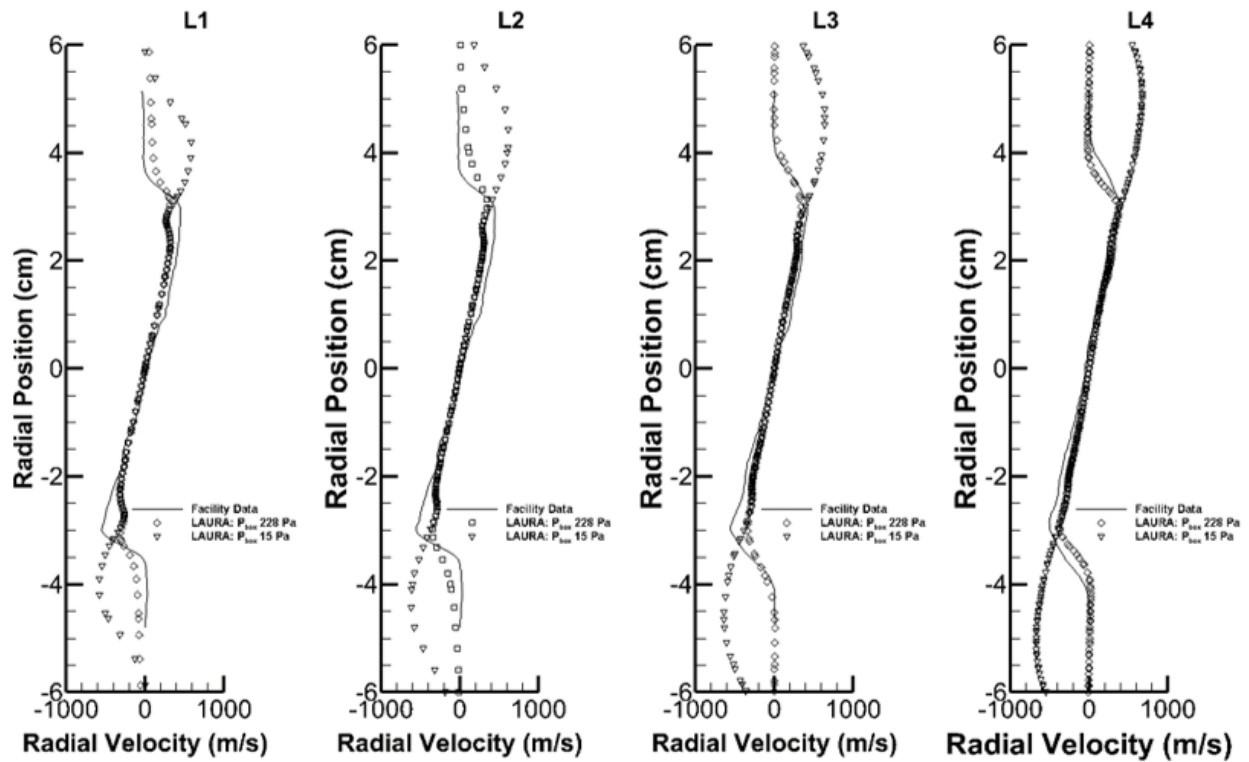


Figure 12: Computed and measured profile distributions of radial velocity: parabolic enthalpy profile, $H_{CL}=10.5$ MJ/kg, $P_{plenum} = 106$ kPa, $P_{box} = 15$ and $P_{box} = 228$ Pa

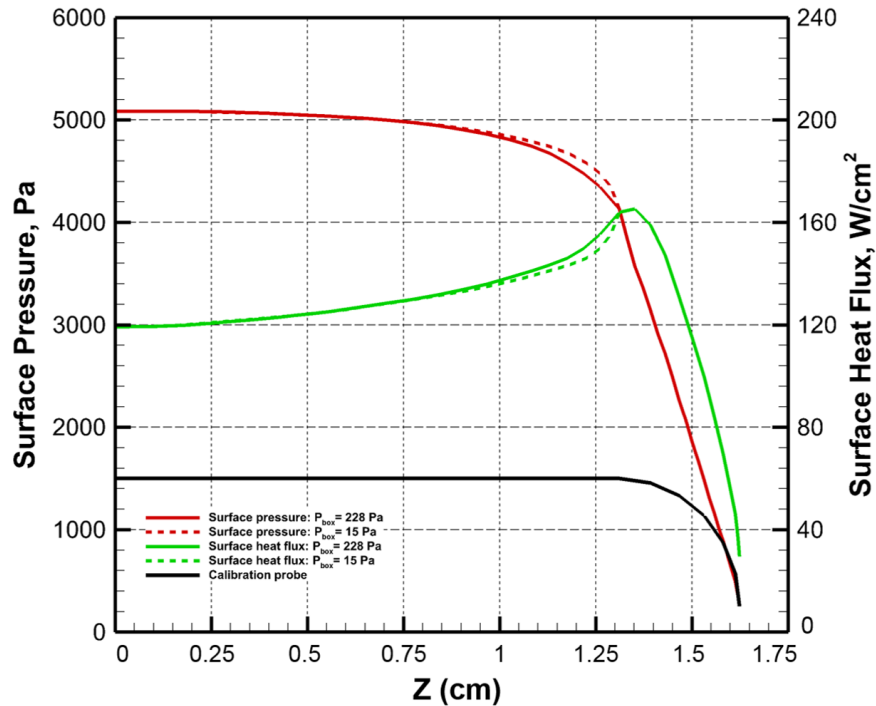


Figure 13: Computed heat flux and pressure profiles along the calibration probe surface at multiple chamber pressures: parabolic enthalpy profile, $H_{CL}=10.5$ MJ/kg, $P_{plenum}= 106$ kPa

V. Arc-jet Calibration Environment

Simulations were performed for a range of arc heater test conditions at low, medium, and high enthalpy, shown in Table 1, to assess the calibrated arc-jet environments measured by calibration probes. The test conditions are labeled with arc heater current setting (in amps) and measured flow rate (in standard liters per minute) that correspond to the lumped plenum total pressure and bulk enthalpy. The inferred enthalpy is estimated using the correlation in Eq. 7 at the corresponding calibrated heat flux and surface pressure values. Once the plenum profiles were established using the approach in Sections III and IV, surface catalysis effects were studied for each test condition from noncatalytic to fully-catalytic conditions to determine the appropriate level of catalysis that best matches the measured calibrated heat flux. (Note that the slug calibration probe is made of copper and typically assumed to be more closely represented by the fully-catalytic condition, but oxidation of the copper slug surface may occur in high enthalpy flows in the arc jet [27].) A fully-catalytic surface has 100% efficiency in promoting atoms and ions species recombination on the surface. On the other hand, noncatalytic surface does not allow species recombination to take place on the surface.

Table 1: Summary of facility parameters, calibrated conditions, and estimated inferred enthalpy for considered test conditions with the 3.3-cm calibration probe

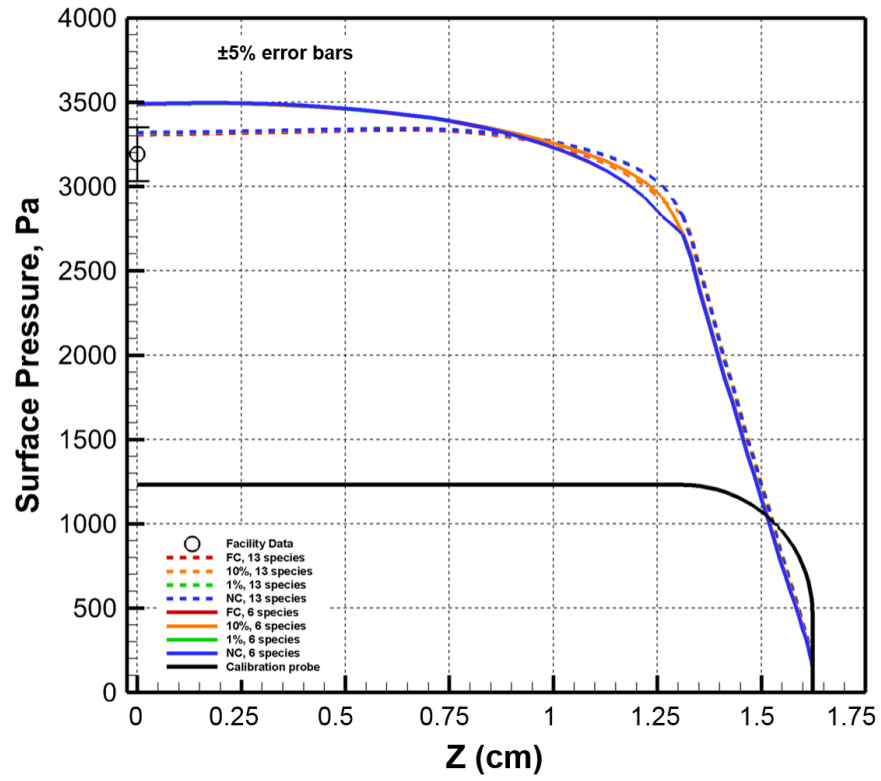
Test Condition	Plenum Total Pressure, kPa	Bulk Enthalpy, MJ/kg	Stagnation Heat Flux, W/cm²	Stagnation Surface Pressure, kPa	Inferred Enthalpy, MJ/kg
100A/400SLPM	109	6.55	107	5.12	9.71
107A/105SLPM	26.8	15.6	170	1.91	25.8
320A/165SLPM	46.7	27.4	332	3.19	38.9

Of the three cases, the 27.4 MJ/kg arc-jet condition is unique in which the stagnation temperature is high enough to trigger some level of ionization in the flow. Therefore, computed surface pressure and heat flux values were compared for 6- and 13-species gas, as shown in Figure 14. In this figure, the calibration probe heat flux and surface pressure profiles for 6-species and 13-species gas are represented with solid and dashed lines, respectively. The results show that the surface pressure and heat flux are impacted by the ions species presence in the flow near the stagnation point, within 0.75 centimeters of the calibration probe centerline. The difference in the results for the surface pressure and heat flux near the stagnation point can be explained by how the presence of 6- and 13-species gas affects the freestream condition upstream of the shock. Recall from the discussion in Section IV that the arc-jet freestream environment upstream of the shock is different from flight, where the atomic and ions species in dissociated gas mixture are vibrationally frozen at a high vibrational temperature upon rapid expansion in the nozzle. Based on the indication of a "hot core" near the nozzle centerline from the inferred enthalpy comparison to the bulk (average) enthalpy

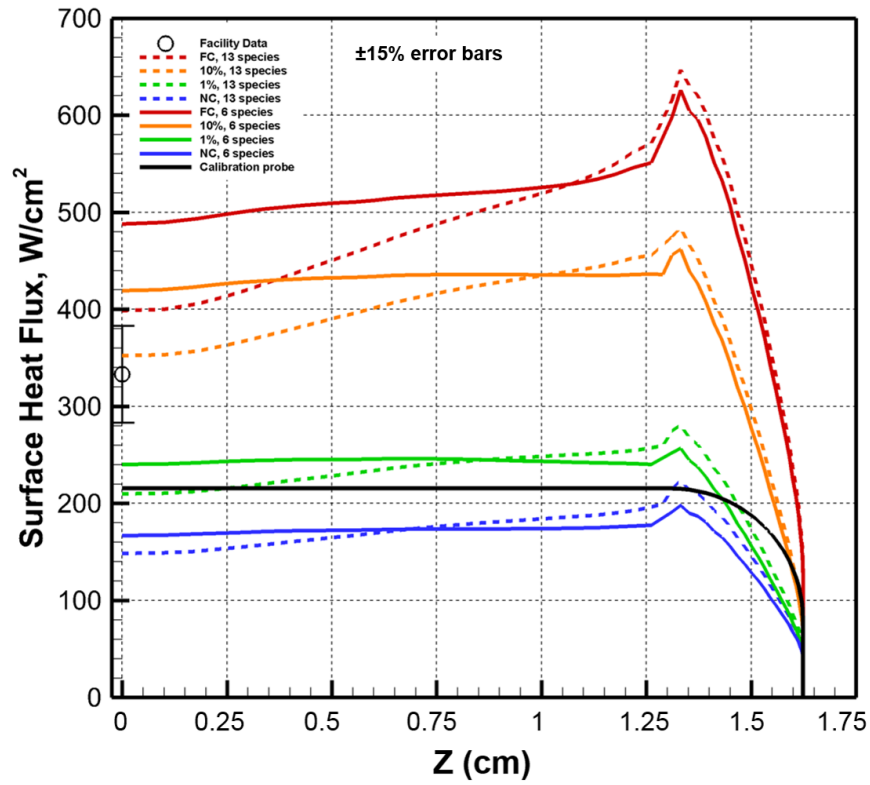
in Table 1, the ions species presence is expected to be near the nozzle centerline and stagnation point. For 13-species gas, the presence of ions species increases the zero-point chemical energy component of the total enthalpy, which results in a decrease in internal molecular energy modes and the gas temperature. As the flow rapidly expands in the diverging section of the nozzle, there is less available energy to be permanently sealed in the frozen vibrational mode and accounts for a smaller portion of the bulk enthalpy at the nozzle exit. Therefore, prior to the shock, there is more available internal energy content and an increase in translational temperature for a 13-species gas. The energy content shift near the nozzle centerline between the 6- and 13-species gas results in changes to the shock stand-off distance and post-shock gradients, which affect the surface pressure and heat flux values on the probe near the stagnation point. Based on the differences observed between the 6- and 13-species gas solutions, 13-species gas was used for the 27.4 MJ/kg arc-jet condition to compare predictions to the calibrated surface values.

Figure 15 shows predicted pressure and heat flux for the 3.3-cm calibration probe at the three calibrated surface heat flux and pressure conditions. The profiles are shown along the calibration probe surface at radial distance, Z , from the center of the probe. The figures on the left show the predicted pressure distributions after adjusting P_{plenum} to match the stagnation pressure to within 5% of the measured Pitot pressure. The CFD results predicted for the heat flux on the calibration probe surface are shown on the right for various catalysis levels. The predicted heat flux and pressure values at the stagnation point (or center) of the calibration probes are compared to the measured values and associated uncertainty [4], designated with error bars.

The plots on the left in Fig. 15 show that the catalysis has negligible impact on the shock location because pressure distributions are nearly identical. However, the variability in the results for the heat flux, shown on the right in Fig. 15, increases as the bulk enthalpy condition and calibrated stagnation heat flux increases. The TPS community, in general, categorizes the catalysis into three bands: effectively fully catalytic, moderately catalytic, and weakly catalytic [27]. From Fig. 15(b), 15(d), and 15(f), the significant impact of the moderately-catalytic band on the surface heat flux can be seen. Between recombination efficiencies of 1 and 10%, the magnitude of the moderately-catalytic band thickens as the bulk enthalpy of the arc-jet flow increases. For example, the surface heat flux profile is less sensitive in the moderately-catalytic band with approximately 25 W/cm² change for the 6.5 MJ/kg case, while the catalytic effect was more significant for the 27.4 MJ/kg case with an increased moderately-catalytic band of about 150 W/cm². Comparing the measured calibrated heat flux to the predicted values, the test data indicates an effectively fully-catalytic surface with 10% recombination efficiency. In Table 2, a summary of the simulated results for the 10% surface catalytic condition is tabulated and compared with the measured heat flux and surface pressure. The predicted surface pressure and heat flux at the stagnation point for 10% recombination

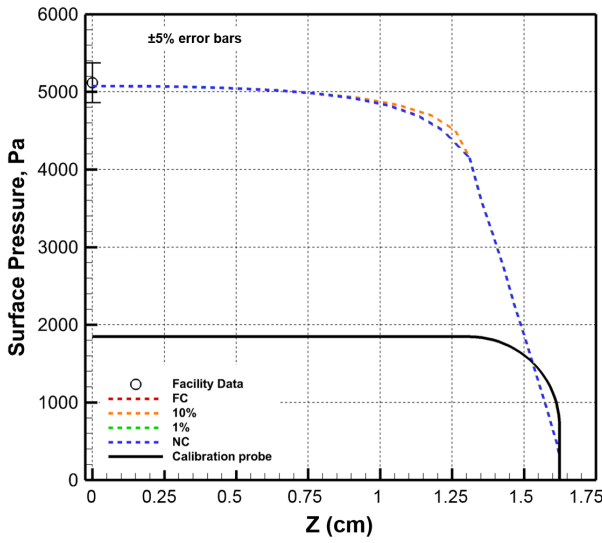


(a)

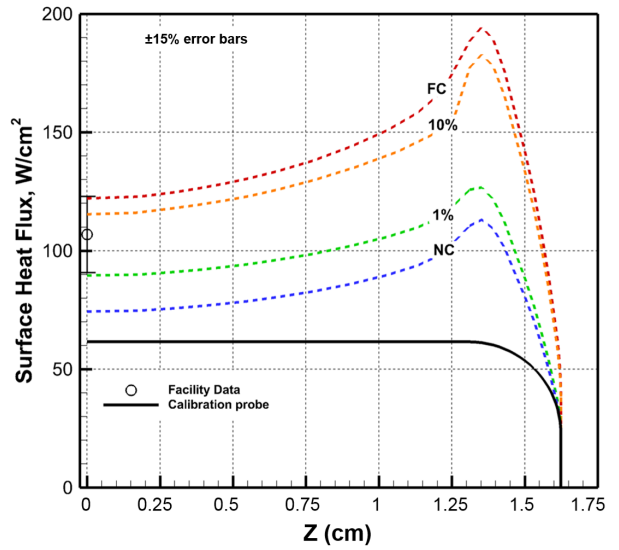


(b)

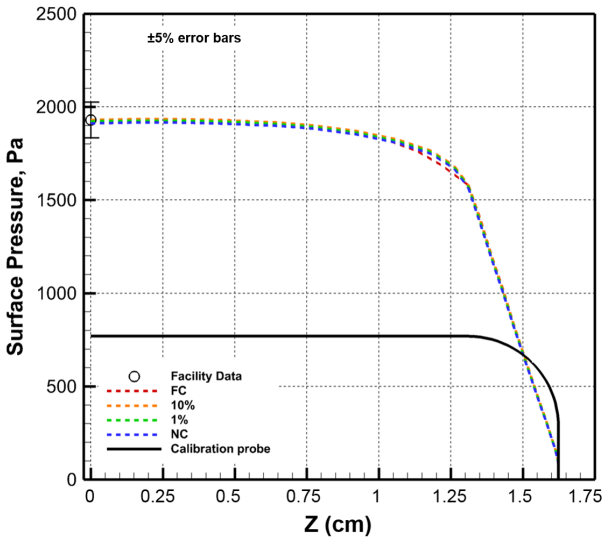
Figure 14: Computational results for the 27.4 MJ/kg condition with 6- and 13-species gas



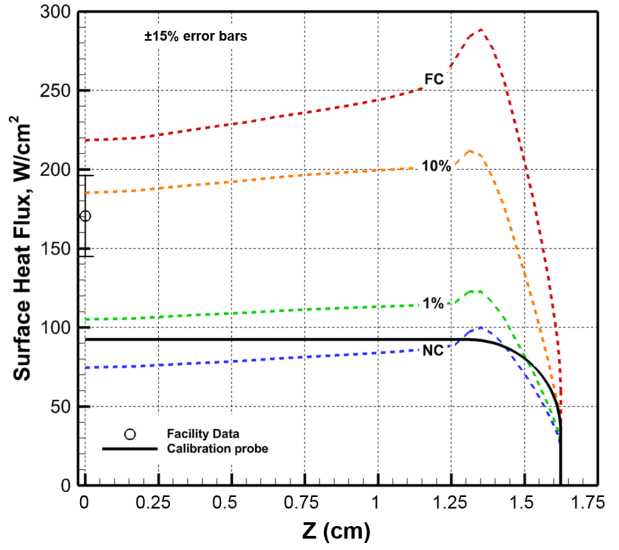
(a)



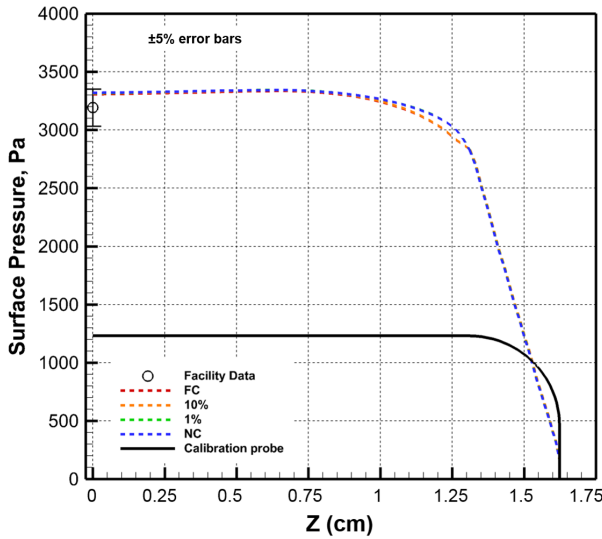
(b)



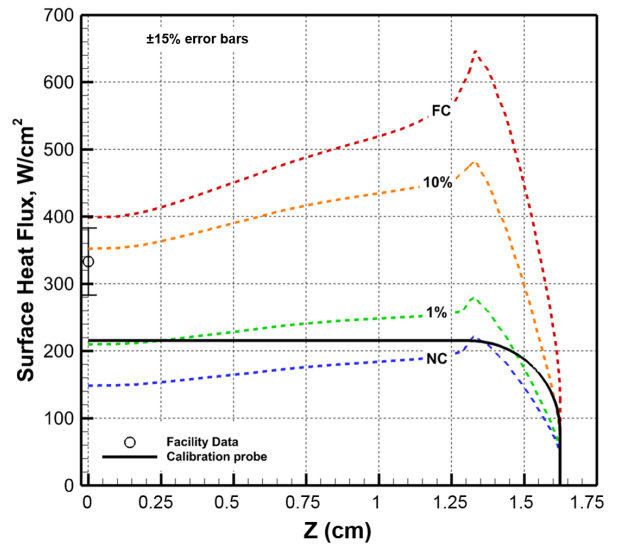
(c)



(d)



(e)



(f)

Figure 15: Computational results for arc-jet conditions tested on the 3.3-cm calibration probe

efficiency agreed well within the measurement uncertainty (5% for Pitot pressure and 15% for slug calorimeter heat flux).

Table 2: Computational results for the 3.3-cm calibration probe at the 10% surface catalytic condition

H_{bulk} , MJ/kg	Stagnation Heat Flux, W/cm ²			Stagnation Surface Pressure, kPa		
	Measured	Predicted	% Diff	Measured	Predicted	% Diff
6.55	107	112	+4.67	5.12	5.09	-0.59
15.6	170	185	+8.82	1.91	1.93	+1.05
27.4	332	352	+6.02	3.19	3.32	+4.07

VI. Conclusions

A method to estimate the arc-jet condition representing the surface calibration probe values was presented. The method involves a three-dimensional model of the arc-jet nozzle and free-jet portion of the flow field and accounts for non-uniform flow-field profiles at the nozzle inlet and surface catalysis effects at the calibration probe surface. The flow-field profiles at the nozzle inlet were determined with an iterative approach to match bulk and inferred enthalpy at the nozzle exit and the surface pressure of the calibration probe. Catalytic effects were studied to determine the appropriate catalytic efficiency level that corresponds to the measured heat flux value. Comparing the CFD results and test data indicates an effectively fully-catalytic copper surface on the heat flux probe of about 10% recombination efficiency and a 2-3 kPa pressure drop from the total pressure measured at the plenum section, prior to the nozzle. With these assumptions, the predictions from the numerical simulations are well within the uncertainty of the stagnation pressure and heat flux measurements. The predicted velocity conditions at the nozzle exit were also compared and agreed with radial and axial velocimetry up to 3 cm from the nozzle centerline. Because the calibration probe sizes are well within this region from the centerline, the cabin pressure has negligible impact on the probe heat flux and pressure values. With the numerical simulations closely representing the measured calibration data, the predictive capability can be used for evaluation of specimens for test planning and ground test correlation to flight.

References

- ¹Wiedemann, K., Clark, R., and Sankaran, S., "Emittance, Catalysis, and Dynamic Oxidation of Ti-14AL-21Nb," Tech. rep., NASA TP-2955, Nov. 1989.
- ²Glass, D., "Oxidation and Emittance Studies of Coated Mo-Re," Tech. rep., NASA CR-201753, Oct. 1997.
- ³Bird, R., Wallace, T., and Sankaran, S., "Development of Protective Coatings for High-Temperature Metallic Materials," *Journal of Spacecraft and Rockets*, Vol. 41, No. 2, 2004, pp. 213-220.

⁴Splinter, S., Bey, K., and Gragg, J., “Comparative Measurements of Earth and Martian Entry Environments in the NASA Langley HyMETS Facility,” AIAA 2011-1014, Jan. 2011.

⁵Prabhu, D., Saunders, D., Oishi, T., Skokova, K., Sanots, J., Fu, J., Terrazas-Salinas, I., Carballo, E., and Driver, D., “CFD Analysis Framework for Arc-Heated Flowfields, I: Stagnation Testing in Arc-Jets at NASA ARC,” AIAA 2009-4080, June 2009.

⁶Mazaheri, A., Bruce, W., Mesick, N., and Sutton, K., “Methodology for Flight-Relevant Arc-Jet Testing of Flexible Thermal Protection Systems,” *Journal of Spacecraft and Rockets*, Vol. 51, No. 3, 2014, pp. 789–800.

⁷Calomino, A., Bruce, W., Gage, P., Horn, D., Mastaler, M., Rigali, D., Robey, J., Voss, L., Wahlberg, J., and Williams, C., “Evaluation of the NASA Arc-Jet Capabilities to Support Mission Requirements,” Tech. rep., NASA SP-2010-577, 1989.

⁸American Society for Testing Materials (ASTM), ., “Standard Test Method for Measuring Heat-Transfer Rate Using a Thermal Capacitance (Slug) Calorimeter,” Tech. rep., ASTM Standard E457-96, 1996.

⁹Nawaz, A. and Santos, J., “Assessing Calorimeter Evaluation Methods in Convective and Radiative Heat Flux Environment,” AIAA 2010-4905, June 2010.

¹⁰American Society for Testing Materials (ASTM), ., “Standard Practice for Measuring Plasma Arc Gas Enthalpy by Energy Balance,” Tech. rep., ASTM Standard E341-81, 1981.

¹¹Mazaheri, M., Gnoffo, P., Johnston, C., and Kleb, B., “LAURA Users Manual: 5.5-64987,” Tech. rep., NASA TM-217800-2013, 2013.

¹²Gupta, R., Yos, J., Thompson, R., and Lee, K., “A Review of Reaction Rates and Thermodynamic and Transport Properties for an 11-Species Air Model for Chemical and Thermal Nonequilibrium Calculations to 30,000 K,” Tech. rep., NASA RP-1232, 1990.

¹³Wright, M., “Recommended Collision Integrals for Transport Property Computations Part 1: Air Species,” *AIAA Journal*, Vol. 43, No. 12, 2005, pp. 2558–2564.

¹⁴Wright, M., “Recommended Collision Integrals for Transport Property Computations Part 2: Mars and Venus Entries,” *AIAA Journal*, Vol. 45, No. 1, 2005, pp. 281–288.

¹⁵Gordon, S. and McBride, B., “Computer Program for Calculation of Complex Equilibrium Compositions and Applications,” Tech. rep., NASA RP-1311, 1994.

¹⁶Brune, A., West, T., Hosder, S., and Edquist, K., “Uncertainty Analysis of Mars Entry Flows over a Hypersonic Inflatable Aerodynamic Decelerator,” *Journal of Spacecraft and Rockets*, Vol. 52, No. 3, 2015, pp. 776–788.

¹⁷Hash, D., Olejniczak, J., Wright, M., Prabhu, D., Pulsonetti, M., Hollis, B., Gnoffo, P., Barnhardt, M., Nompelis, I., and Candler, G., “Fire II Calculations for Hypersonic Nonequilibrium Aerothermodynamics Code Verification: DPLR, LAURA, and US3D,” AIAA 2007-0605, Jan. 2007.

¹⁸Mazaheri, M. and Wood, W., “Re-Entry Aeroheating Analysis of Tile-Repair Augers for the Shuttle Orbiter,” AIAA 2007-4148, June 2007.

¹⁹Mazaheri, A. and Wood, W., “Heating Augmentation for Short Hypersonic Protuberances,” *Journal of Spacecraft and Rockets*, Vol. 46, No. 2, 2009, pp. 284–291.

²⁰Dyakonov, A., Schenenberger, M., Scallian, W., Van Norman, J., Novak, L., and Tang, C., “Aerodynamic Interference Due to MSL Reaction Control System,” AIAA 2009-1030, Jan. 2009.

²¹Johnston, C., Gnoffo, P., and Mazaheri, A., “A Study of Ablation-Flowfield Coupling Relevant to the Orion Heatshield,” AIAA 2009-4318, June 2009.

²²Mazaheri, A., “HEART Aerothermodynamic Analysis,” Tech. rep., NASA TM-2012-217568, 2012.

²³Smith, D. and Carver, D., “Flow Calibration of Two Hypersonic Nozzles in the AEDC Heat-H2 High-Enthalpy Arc-Heated Wind Tunnel,” AIAA 1993-2782, 1993.

²⁴Heister, N. and Clark, C., “Feasibility of Standard Evaluation Procedures for Ablating Materials,” Tech. rep., NASA CR-379, 1966.

²⁵Heister, N. and Clark, C., “Comparative Evaluation of Ablating Materials in Arc Plasma Jets,” Tech. rep., NASA CR-1207, 1968.

²⁶Inman, J., Bathel, B., Johansen, C., Danehy, P., Jones, S., Gragg, J., and Splinter, S., “Nitric Oxide PLIF Measurements in the Hypersonic Materials Environmental Test System (HyMETS),” AIAA 2011-10190, Jan. 2011.

²⁷Nawaz, A., Driver, D., Terrazes-Salinas, I., and Sepka, S., “Surface Catalysis and Oxidation on Stagnation Point Heat Flux Measurements in High Enthalpy Arc Jets,” AIAA 2013-3138, 2013.